Assorted analytical and spectroscopic techniques for the optimization of the defects related properties in size-controlled ZnO nanowires

Kin Mun Wong,[†,a] Yaoguo Fang,[†,ab] André Devaux,[c] Liaoyong Wen,[a] Jian Huang,[b] Luisa De Cola,[c] and Yong Lei[*a]

[a]*Institute of Materials Physics and Center for Nanotechnology, University of Muenster, Wilhelm-Klemm-Str. 10, 48149 Muenster, Germany*

[b]*Institute of Nanochemistry and Nanobiology, School of Environmental and Chemical Engineering, Shanghai University, Shanghai 201800, People's Republic of China*

[c]*Physical Institute and Center for Nanotechnology, CeNTech, Westfälische Wilhelms-Universität Münster, D-48149, Münster, Germany*

Supplementary Information

1. Description of the Equipment used for the various spectroscopic characterization

The surface morphology and structure of the ZnO NWs prepared by the aqueous solution method and the CVD process were characterized by a JEOL JSM-6700F field emission scanning electron microscopy (FESEM) and the microsturctural characterization of the NWs were performed using a JEOL JEM-2010F transmission electron microscope (TEM). On the other hand, the surface and bulk chemical composition of the samples were analyzed by a PHI-5000C ESCA system with Mg K_α x-ray radiation source (where $h\nu = 1253.6\,\text{eV}$) and an Oxford INCA EDS module attached to the FESEM, respectively. The CPL intensity mapping on the submicrometre scale and the temporal decay of CPL were performed using a PicoQuant MicroTime 200 confocal microscope. In the present study, all the CPL measurements were carried out at room temperature and the luminescence of the ZnO NWs samples was excited with a pulsed diode laser at 375 nm and at a constant intensity. A single-photon avalanche diode detector from MPD as well as a PicoHarp 300 were utilized for acquiring the count of the time correlated single photon, and the data was analyzed with the SymPhoTime software package from PicoQuant (version 5.13). On the other hand, additional

PL measurements were also performed with the use of a Hitachi F-7000 fluorimeter. The structural and residual stress data in the NWs was obtained by X-ray diffraction (XRD) measurements using a D/MAX-2550 diffractometer (from Rigaku, Japan) which is equipped with a rotating anode and a Cu K_α radiation source where $\lambda = 1.54178$ Å. Conversely, the $I-V$ measurements on the ZnO NWs arrays were conducted using a Veeco DI 3100 multimode scanning probe system (SPM) with conductivity measurement capability.

On the other hand, the Hall measurement was performed on the ensembles of ZnO nanowires (NWs) arrays and was not performed on an individual ZnO NW. The Hall measurements on the ZnO NWs arrays was carried out at room temperature by using the Van der Pauw four probe technique[1] with a square configuration utilizing an Accent HL5500 system. A thin aluminium (Al) foil (same size as the ZnO NWs arrays sample) with a circular hole (radius is about 0.1 cm) very close to each of the four corners was used as a mask, for the subsequent physical vapour deposition of a mixture of gold-zinc (Au-Zn) powder for the formation of the Au-Zn electrodes on top of the ZnO NWs arrays. After the Au-Zn electrodes were each deposited at the four corners of the ZnO NWs arrays sample, the Al foil was removed where the sample area consisting of the ZnO NWs arrays is about 1 x 1 cm^2 and the area of each Au-Zn electrode is about 0.03 cm^2. Subsequently, annealing of the ZnO NWs arrays sample with the four Au-Zn electrodes was performed in nitrogen gas at the temperature of 500 ^oC for 1 minute. This annealing step was performed as the Au-Zn contacts would become ohmic with a low resistivity value when annealed at 500 ^oC in nitrogen ambient.[2] Moreover, good ohmic contacts between the electrodes and the ZnO NWs was confirmed before the Hall measurements. Therefore the carrier concentration obtained from the Hall measurements refers to the ensembles of synthesized ZnO NWs arrays which is assumed to be the same for each individual ZnO NW. Please refer to Fig. S1 for the schematic diagram illustrating the experimental setup of a square configuration for the Hall

measurements on the ZnO NWs arrays.

A very recently published article in the journal Nanoscale[3] uses a similar Van der Pauw sample configuration to measure the carrier concentration of ZnO NWs arrays. In addition, there are also other reports which use the Hall method to measure the carrier concentration of ZnO NWs arrays.[4-7] On the other hand, it has also been hypothesized that the Hall method may be applicable to ZnO NWs if the diameter of the NW is greater than 30 nm since the quantum confinement effects are negligible in the radial direction and the NWs are still expected to exhibit three-dimensional electron transport properties.[8] For our samples, the diameters of the ZnO NWs are bigger than 30 nm as seen from the cross-sectional SEM images in Fig. 2 (in the manuscript).

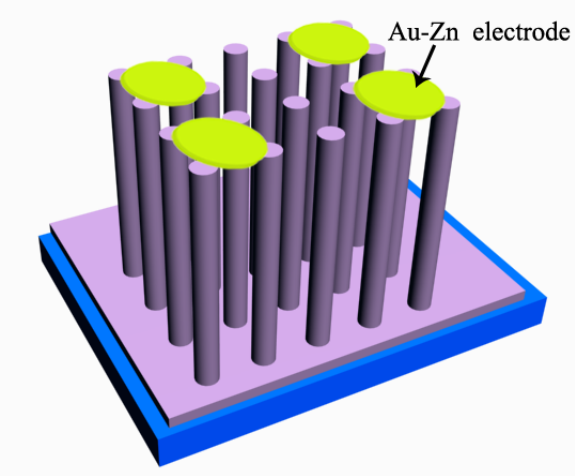

Fig. S1 Schematic diagram of the ZnO NWs arrays sample with the Au-Zn electrodes for the Hall measurements.

2. XRD analysis of the ZnO NWs

The crystalline quality of the ZnO NWs samples were investigated by x-ray diffraction and Fig. S2 shows the XRD pattern for the as-prepared ZnO NWs arrays in all the four samples. Only two diffraction peaks were observed where the peak of the stronger diffraction corresponds to the plane (002) and the second weaker diffraction peak to the (004) plane. The occurrence of the two peaks corresponding to the (002) and (004) plane and the absence of

any other peaks in the XRD pattern indicates preferential orientation of the ZnO NWs along the [0001] direction with their c-axis perpendicular to the substrate.[9]

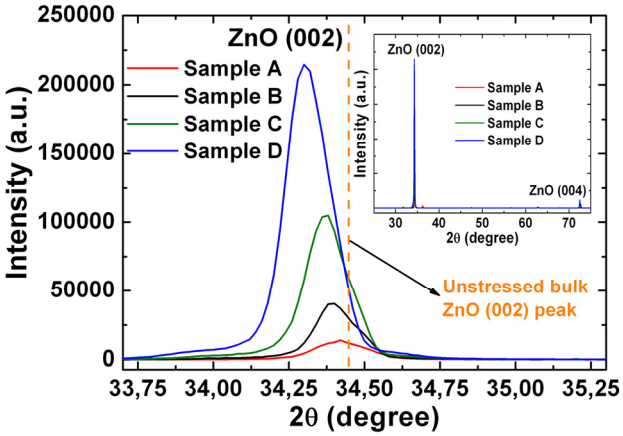

Fig. S2 XRD pattern of the ZnO nanowires in the four samples A to D. The inset shows the spectra over a wider range of 2θ.

In the longest ZnO NWs arrays (sample D), the angular position of the ZnO (002) peak is located at $2\theta = 34.29^{o}$ while it shifts towards $2\theta = 34.40^{o}$ for the shortest ZnO NWs (sample A). This implies that there is some relaxation of the residual stress in the crystal lattice of the shortest NWs as the (002) peak for unstressed bulk ZnO is located at $2\theta = 34.44^{o}$.[10] The origin of the main component of the residual stress has been attributed to the intrinsic stress due to the presence of intrinsic point defects (e.g. V_o, Zn_i) incorporated in the crystal lattice during the growth process[11] and has been shown to be compressive in nature.[12] The other component of the residual stress is attributed to the thermal stress due to the difference in the thermal expansion coefficient of ZnO ($4.75x10^{-6}K^{-1}$) and the Si substrate ($2.60x10^{-6}K^{-1}$), however it is much smaller in magnitude as compared to the intrinsic stress.[13] This shift of the ZnO (002) peak towards smaller values of $2\theta = 34.30^{o}$ (away from $2\theta = 34.44^{o}$) for the NWs in sample D implies that the longer ZnO NWs contains a higher concentration of zinc interstitials or oxygen vacancies. This could be possibly due to a larger incorporation of the zinc atoms into the NWs during the longer synthesis time required for the NWs using the CVD process (which is also in agreement with the XPS and

EDS analysis in section 3.2), hence leading to a higher concentration of Zn_i and compressive stress stemming from them.[12] In addition, assuming a homogeneous stress in the NWs, the Scherrer formula[14] can be used to estimate the grain size from the full width at half maximum (FWHM) of the (002) diffraction peak. The monotonic increase of the FWHM of the ZnO (002) diffraction peak in Fig. S2 as the length of the NWs is increased indicates a decrease in the grain size which also signifies a poorer crystalline quality of the longer ZnO NWs.[15]

3. EDS spectrum of the synthesized ZnO NWs

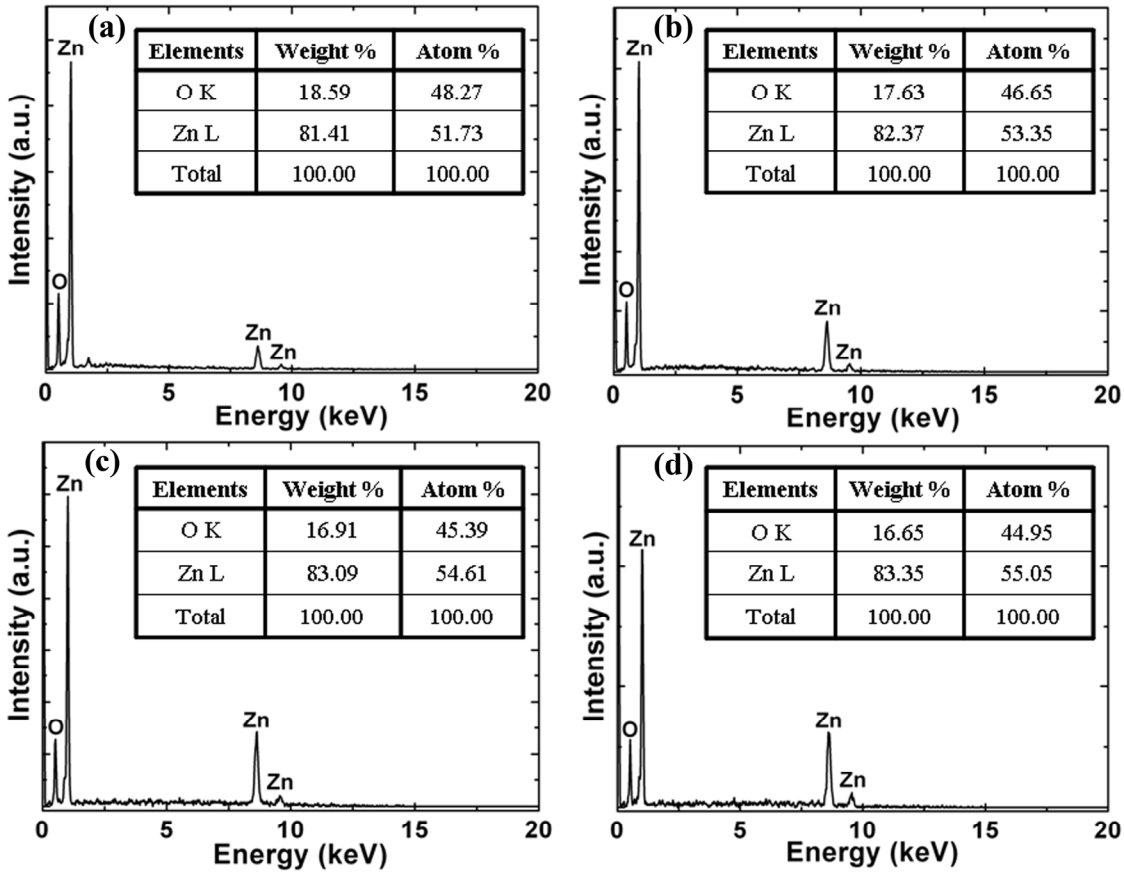

Fig. S3 EDS spectra of the ZnO nanowires in the sample (a) A, (b) B, (c) C and (d) D.

4. Further description about the oxygen vacancies, comparison between the PL and CPL spectra as well as the linear relationship between the integrated CPL spectra and the excitation intensity for the ZnO NWs

The oxygen vacancies can occur in three charge states which is the neutral oxygen vacancy (V_o^n), the singly ionized oxygen vacancy (V_o^+) and the doubly ionized oxygen vacancy (V_o^{++}). They are neutral, singly positive charged and doubly positive charged with respect to the ZnO lattice as the trap has captured 2 electrons, 1 electron and no electrons, respectively. However, there is still some uncertainty on the exact recombination model of the green emission involving the oxygen vacancies. For instance, it could be due to the electronic transition between the singly ionized V_o with photoexcited holes[16] or a recombination of the delocalized electrons near to the conduction band with the doubly ionized V_o centers.[17] Recently, a model combining some of the above-mentioned mechanisms has also been proposed.[18]

On the other hand, the smoother PL spectrum as compared to the CPL spectra corresponding to the samples in Figs. 6(b) and 6(a) (in the manuscript), respectively, is because the observed PL intensity in Fig. 6(b) represents an average over a larger number of NWs as compared to the CPL intensity [in Fig. 6(a)] which is only due to the individual NW over the excitation laser spot area, hence the signal to noise in the PL intensity [in Fig. 6(b)] is reduced. (On the other hand, the disappearance of the CPL band centered at 400 nm and 420 nm [in Fig. 6(a)] could be due to the cut-off filter used in the CPL measurements to remove the laser light where the filter also removes all emission between 400 nm and 420 nm.)

By integrating the area under 3 different CPL spectra (figures not shown) obtained by varying the excitation intensity at 375 nm corresponding to the ZnO NWs array in sample C, a linear correlation is observed as shown in Fig. S4 between the spectrally integrated CPL curves and the increase of the excitation intensity. (Unfortunately, the photodiode which measures the intensity of the excitation laser before it reaches the sample is uncalibrated, and

hence the unit of the excitation intensity is unknown but the relative excitation intensity was doubled for each measurement on sample C). Since the CPL intensity consists mainly of the green band, the linear relationship[16] observed in Fig. S4 indicates that the range of applied light intensity used in the experiments does not influence the concentration of the V_o defects responsible for the green emission on the surface as well as in the annulus region of the as-synthesized NWs.

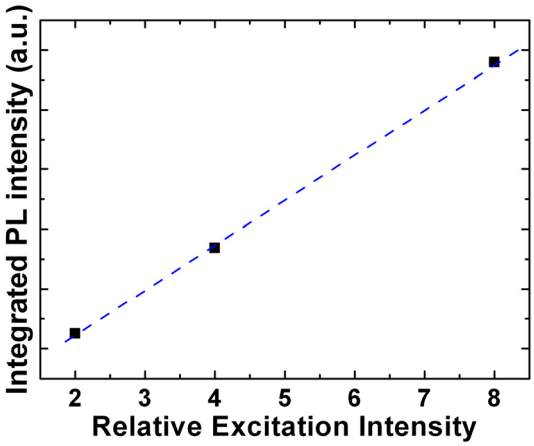

Fig. S4 Plot of the spectrally integrated CPL intensity as a function of relative excitation intensity.

5. Redshift of the CPL and PL emission spectra in the size-controlled ZnO NWs

Under the same excitation wavelength of 375 nm in Fig. 6(a) (in the manuscript), besides the difference in the relative intensity, the peak positions of the 4 peaks also exhibit a small red shift of about 23 nm (from about 499 nm to 522 nm) among themselves. This red-shift of 109 meV as observed in Fig. 6(a) suggests that the energy of the electronic transitions for the green PL emission is slightly reduced. Similarly, a redshift of the emission spectra is also observed in Fig. 6(b) for the four samples corresponding to the excitation wavelength of 270 nm. Generally, two mechanism which could account for the observed red shift are the variation of the oxygen-vacancy concentration in the NWs[19] or the build up of generated internal stress due to the presence of intrinsic defects in the NWs, where it could lead to a

reduction of the bandgap.[20] If the ZnO NW is approximated as a solid cylinder then from Lamé's equations, both the circumferential stress (hoop stress) and radial stress is constant throughout the interior of the NW.[21] Furthermore, since the amount of internal stress can lead to a narrowing of the bandgap,[20] if there is no significant shift of the energy levels of the deep level defects such as V_o with respect to the band edge, then the sample will respond optically by emitting at lower energy due to the narrowing of the bandgap. Although the amount of intrinsic residual stress in the NW is constant in an individual sample (from the above approximation), this residual stress level can change between samples. Some evidence in support of this is indicated in the XRD result in Fig. S2 which shows that there is some intrinsic residual stress present in the synthesized NWs due to point defects. In addition, the amount of intrinsic residual stress is correlated with the concentration of intrinsic defects in the ZnO NWs (from Fig. S2). For example, sample D possesses the largest amount of intrinsic residual stress [in Fig. S2] (due to the largest concentration of intrinsic defects) displays the biggest red-shift in the green band PL as shown in Fig. 6(a). Hence, the redshift of the PL and CPL spectra in Figs. 6(a) and 6(b), respectively, at the same excitation wavelength could be probably due to the different constant level of intrinsic residual stress in the different samples.

However by comparing Figs. 6(a) and 6(b), it is also observed that all four samples also redshift when the excitation wavelength increases from 270 nm to 375 nm and Fig. S5 shows the red-shift for each individual sample. To explain this phenomenon, a longer excitation wavelength (smaller photon energy) corresponds to a slightly shallower penetration depth in the samples, and the intrinsic stress is assumed to be constant throughout the NW in an individual sample (from the assumption that the NW is a solid cylinder and Lamé's equations[21]). Hence we could infer that a probable cause for the redshift in an individual sample when the excitation wavelength increases could be due to some spatial variation of the concentration of V_o defects beneath the NW surface (since V_o could also cause the green PL

band to red-shift[19]). This is in agreement with the earlier discussion between the correlation of the XPS and EDS results with the changes in the magnitude of the PL and CPL spectra.

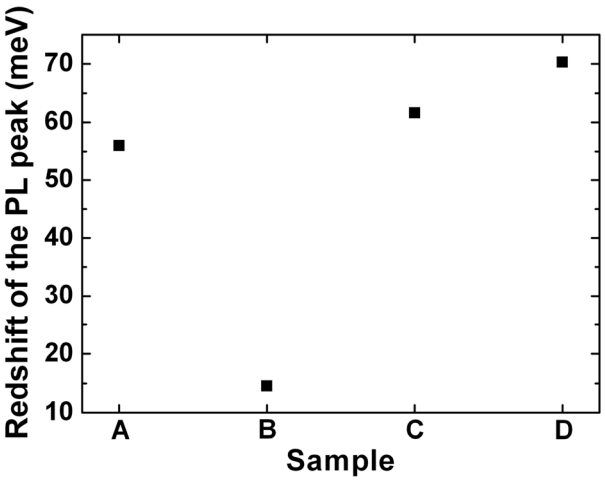

Fig. S5 The redshift of the green band in meV between the PL and CPL spectra corresponding to the four samples with the change in the excitation wavelength from 270 nm to 375 nm.

6. Influence of the S/V ratio on the radiative lifetime of the ZnO NWs

It has been observed in experimental studies that the radiative lifetime in ZnO NWs exhibits size dependence where the exciton radiative lifetime increases with the size of the ZnO nanostructures and is related to the exciton-polariton effects.[22] It was also theorized that the quantization of the wave vector in the vertical direction inside a nanostructure would decrease the number of possible wave vectors, thus leading to an increase of the radiative recombination time.[23]

Recently, it has been suggested that the radiative lifetime of ZnO nanostructures could be related to the radiative lifetime of the free excitons.[24] For our ZnO NWs, the top view of the SEM images in Fig. 2 (in the manuscript) show that the average size of the NWs increases when its length increases and as calculated from eqn (1), this results in a decreasing S/V ratio (Table 2). Consequently, for our synthesized ZnO NWs as its length increases, the corresponding decreasing S/V ratio could lead to a decrease of the scattering rate of the excitons with the surface of the ZnO NWs, which would then increase the radiative lifetime

due to some surface recombination process.[25] To exemplify this point, by fitting a straight line through the data points in Fig. S6, a comparison of the slope of the decay rate between our samples and with the NWs (with diameter between 29 nm to 40 nm) from Hong *et al.* (Ref. 22) can be made. The comparison shows that the slope of the decay rate for our samples is comparatively much smaller (by two orders of magnitude) which indicates a slower scattering rate with the surface. Hence the correlation between the increase of the radiative lifetime with the increase of the length of our ZnO NWs [in Table 2] could be possibly due to the decrease of the S/V ratio which induces a lower scattering rate with the surface. However, the above mentioned mechanism is surface related which is different from the quantum confinement effect (QCE) which does not have a pronounced effect on our samples. It is known that QCE also lead to size dependent oscillator strength which increases the radiative lifetime of ZnO nanostructures as its size increases.[26] However for our samples, the QCE is negligible as the range of diameters of our synthesized ZnO NWs are much bigger than the Bohr radius of exciton in ZnO (1.8 nm).[27]

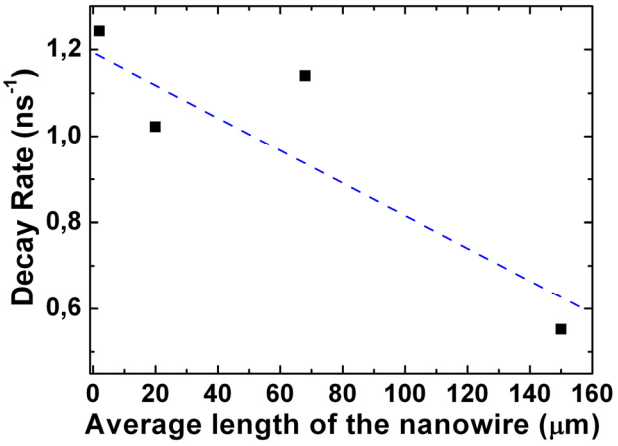

Fig. S6 CPL decay rate versus the length of the ZnO nanowires where the linear fitting (dashed line) is also plotted in the figure.

Interestingly, a decrease in the radiative lifetime depending on the observed increase of the CPL intensity (due to the increase of the concentrations of the oxygen vacancies), corresponding to the longer ZnO NWs was not observed. This could probably be due to the

trade-off between the higher concentration of the oxygen vacancies and the decrease of the scattering rate of the excitons due to the smaller S/V ratio corresponding to the longer ZnO NWs, since the former will decrease while the later will increase the radiative lifetime. On the other hand, the relatively long radiative lifetime of the as-synthesized ZnO NWs (in the range of ns) could be due to the localization of the excitons bound to the surface which could result in some elimination of the faster radiative channels.[28]

7. Full derivation of the analytical model for the calculation of the donor concentration of the ZnO NWs from its corresponding I-V characteristics

At room temperature and for reverse bias voltage, the tunnelling current is predominantly due to the thermionic field emission current[29] and the current density through ϕ_{Pt-NW} is given by[29]

$$J_{Pt-NW} = \frac{A^{**}T}{k}\sqrt{\pi E_{oo} q[V_R + \frac{\phi_{Pt-NW}}{\cosh^2(E_{oo}/kT)}]}\exp(\frac{-q\phi_{Pt-NW}}{E_o})\exp(\frac{qV_R}{\varepsilon'}) \quad (1)$$

where

$$\varepsilon' = \frac{E_{oo}}{(E_{oo}/kT) - \tanh(E_{oo}/kT)} \quad (2)$$

and

$$E_o = E_{oo}\coth(\frac{E_{oo}}{kT}) \quad (3)$$

where E_{oo} is the characteristic energy relating to the tunnelling probability given by

$$E_{oo} = \frac{qh}{4\pi}\sqrt{\frac{N_d}{m_e^* \varepsilon_s}} \quad (4)$$

In Eq. (1), A^{**} is the reduced effective Richardson constant which takes into account of the effects of optical-phonon scattering and quantum mechanical reflection.[29] $\varepsilon_s = \varepsilon_r \varepsilon_o$ is the

permittivity of the ZnO NW, $\varepsilon_r = 8.36$[30] is the relative permittivity of the ZnO NW used in this study (corresponding to thin ZnO film as the quantum confinement effects in our ZnO NW is not significant because r_{NW} is larger than the ZnO exciton Bohr radius[27]) and ε_o is the permittivity of free space. N_d is the donor concentration in the ZnO NW expressed in m^{-3}. It should be clarified that in Eq. (1), ϕ_{Pt-NW} is in volts. Substituting Eq. (2) into the $\exp(\frac{qV_R}{\varepsilon'})$ term of Eq. (1) and simplifying result in

$$\exp(qV_R * \frac{1}{\varepsilon'}) = \exp[\frac{qV_R}{kT} - \frac{qV_R \tanh(E_{oo}/kT)}{E_{oo}}] \quad (5)$$

using $\tanh(\frac{E_{oo}}{kT}) = \frac{1}{\coth(\frac{E_{oo}}{kT})}$ and Eq. (3), Eq. (5) can be further simplified as

$$\exp(\frac{qV_R}{\varepsilon'}) = \exp[\frac{qV_R}{kT} - \frac{qV_R}{E_{oo}\coth(E_{oo}/kT)}] = \exp(\frac{qV_R}{kT} - \frac{qV_R}{E_o}) \quad (6)$$

Substituting Eq. (6) back into Eq. (1), the current density through the reverse biased Schottky barrier at the probe tip-ZnO NW interface, ϕ_{Pt-NW} is given by

$$J_{Pt-NW} = \frac{A^{**}T}{k}\sqrt{\pi E_{oo} q[V_R + \frac{\phi_{Pt-NW}}{\cosh^2(E_{oo}/kT)}]}\exp(\frac{-q\phi_{Pt-NW}}{E_o})\exp[\frac{qV_R}{kT} - \frac{qV_R}{E_o}] \quad (7)$$

Taking the natural logarithms on both sides of Eq. (7) where $J_{Pt-NW} = \frac{I_{Pt-NW}}{A_{Pt-NW}}$ and A_{Pt-NW} is the effective contact area for the Schottky barrier at the probe tip-ZnO NW interface, we have

$$\ln(\frac{I_{Pt-NW}}{A_{Pt-NW}}) = \ln(\frac{A^{**}T\sqrt{\pi E_{oo} q}}{k}) + \frac{1}{2}\ln[V_R + \frac{\phi_{Pt-NW}}{\cosh^2(E_{oo}/kT)}] - \frac{q\phi_{Pt-NW}}{E_o} + \frac{qV_R}{kT} - \frac{qV_R}{E_o} \quad (8)$$

The current transport mechanism in the ZnO NW is dependent on the parameter E_{oo} and as discussed earlier, the current through the reverse biased Schottky barrier at the probe tip-ZnO NW interface, ϕ_{Pt-NW} is primarily due to the thermionic field emission,[29] hence $E_{oo} \approx kT$[29] and Eq. (8) can be further simplified as

$$\ln(I_{Pt-NW}) = \ln(\frac{A^{**}T\sqrt{\pi kTq}}{k}) + \frac{1}{2}\ln[V_R + \frac{\phi_{Pt-NW}}{\cosh^2(1)}] - \frac{q\phi_{Pt-NW}}{E_o} + \frac{qV_R}{kT} - \frac{qV_R}{E_o} + \ln(A_{Pt-NW}) \quad (9)$$

The term $\frac{1}{2}\ln[V_R + \frac{\phi_{Pt-NW}}{\cosh^2(1)}]$ in Eq. (9) can be rewritten as

$$\frac{1}{2}\ln[V_R + \frac{\phi_{Pt-NW}}{\cosh^2(1)}] = \frac{1}{2}\ln\{\frac{\phi_{Pt-NW}}{\cosh^2(1)}[\frac{\cosh^2(1)}{\phi_{Pt-NW}}V_R + 1]\}$$

$$= \frac{1}{2}\ln[\frac{\phi_{Pt-NW}}{\cosh^2(1)}] + \frac{1}{2}\ln[\frac{\cosh^2(1)}{\phi_{Pt-NW}}V_R + 1] \quad (10)$$

Hence Eq. (8) can be further expressed as

$$\ln(I_{Pt-NW}) = \ln(\frac{A^{**}T\sqrt{\pi kTq}}{k}) + \frac{1}{2}\ln[\frac{\phi_{Pt-NW}}{\cosh^2(1)}] + \frac{1}{2}\ln[\frac{\cosh^2(1)}{\phi_{Pt-NW}}V_R + 1] - \frac{q\phi_{Pt-NW}}{E_o} + \frac{qV_R}{kT} - \frac{qV_R}{E_o} + \ln(A_{Pt-NW}) \quad (11)$$

To obtain a mathematical expression in Eq. (11) which permits further algebraic evaluation, the Padé approximant technique will have to be considered where the rational function, $P(x)_{[m/n]}$ representing the Padé approximant of order $[m/n]$ (where m and n are two integers ≥ 0) for the function of $\ln(x+1)$ is given by[31]

$$P(x)_{[2/1]} = \frac{x^2 + 6x}{4x + 6} \approx \ln(1+x) \quad (12)$$

The use of the Padé approximant provides better and fast approximation with a lower root mean square error of the function $\ln(x+1)$ as compared to the poorly converging Taylor series of $\ln(x+1)$. This is mainly due to the alternating terms in the Taylor series expansion of $\ln(x+1)$ which leads to a very poor convergence of the power series. On the other hand, the rational function in Eq. (12) can be expressed as a sum of a polynomial and a proper rational term given by

$$\ln(x+1) \approx \frac{x}{4} + \frac{9}{8} - \frac{27}{8(2x+3)} \quad (13)$$

As a result, from Eq. (13), the $\frac{1}{2}\ln[\frac{\cosh^2(1)}{\phi_{Pt-NW}}V_R+1]$ term in Eq. (11) can be expressed as

$$\frac{1}{2}\ln[\frac{\cosh^2(1)}{\phi_{Pt-NW}}V_R+1]=\frac{\cosh^2(1)}{8\phi_{Pt-NW}}V_R+\frac{9}{16}-\frac{27\phi_{Pt-NW}}{32\cosh^2(1)V_R+48\phi_{Pt-NW}} \quad (14)$$

By substituting Eq. (14) back into Eq. (11) and grouping the like terms with the variable "V_R" together, the reverse bias thermionic field emission current through the Schottky barrier at the probe tip-ZnO NW interface can be finally expressed as

$$\ln(I_{Pt-NW})=[\frac{\cosh^2(1)}{8\phi_{Pt-NW}}+\frac{q}{kT}-\frac{q}{E_o}]V_R-\frac{27\phi_{Pt-NW}}{32\cosh^2(1)V_R+48\phi_{Pt-NW}}+\ln(\frac{A^{**}T\sqrt{\pi kTq}}{k})+\frac{1}{2}\ln[\frac{\phi_{Pt-NW}}{\cosh^2(1)}]+\frac{9}{16}-\frac{q\phi_{Pt-NW}}{E_o}+\ln(A_{Pt-NW}) \quad (15)$$

Before proceeding further in the derivation of the analytical equation for obtaining the donor concentration of the ZnO NW directly from the $\ln I-V$ characteristics, it is necessary to consider the influence of the second rational term, $T(V_R)=-\frac{27\phi_{Pt-NW}}{32\cosh^2(1)V_R+48\phi_{Pt-NW}}$ in Eq. (15). The asymptote of the $T(V_R)$ term occurs at $V_{R|asym}=-\frac{3\phi_{Pt-NW}}{2\cosh^2(1)}$ and since in the CAFM measurements, a platinum coated probe tip is used where the Schottky barrier height at the interface between the Pt probe tip and the top of the ZnO NW is typically between 0.40 eV and 0.93 eV.[32] Hence the value of $\phi_{Pt-NW}<\cosh^2(1)$ which implies that $\frac{\phi_{Pt-NW}}{\cosh^2(1)}\ll 1$, as a result the value $V_{R|asym}$ (assuming the largest value of at 0.93eV) will be smaller than 0.6 V. In addition, the gradient of the rational term given by

$$\frac{dT}{dV_R}=-\frac{864\phi_{Pt-NW}\cosh^2(1)}{[32\cosh^2(1)V_R+48\phi_{Pt-NW}]^2} \quad (16)$$

and at V_R = -1V and -2 V, the magnitude of the gradient of the curve is at 1.921 and 0.165, respectively, where this translates to a decrease of about 91 % of the magnitude of the gradient of the curve at V_R = -2V as compared to V_R = -1V. Therefore the influence of the

rational term, $T(V_R)$ will be minimal on the reverse biased $\ln(I)-V_R$ characteristics when $V_R < -2$ V. On the other hand, in Eq. (15), besides the V_R term and $T(V_R)$ term, the other terms in the equation do not involve the variable "V_R" and are constants.

Therefore using Eq. (15), an equation for calculating the donor concentration directly from the slope of the reverse bias $\ln I_R - V_R$ characteristics (denoted as G_R), obtained from the reverse bias $I_R - V_R$ characteristics in Fig. 9(b) corresponding to the ZnO NW is given by

$$\frac{\cosh^2(1)}{8\phi_{Pt-NW}} + \frac{q}{kT} - \frac{q}{E_o} = G_R \tag{17}$$

As previously discussed when the current transport mechanism is dominated by thermionic field emission, $E_{oo} \approx kT$ and E_o in Eq. (3) is approximately equal to $E_{oo}\coth(1)$ hence,

$$\frac{\cosh^2(1)}{8\phi_{Pt-NW}} + \frac{q}{kT} - \frac{q}{E_{oo}\coth(1)} = G_R \tag{18}$$

and rearranging the above equation,

$$E_{oo} = \frac{q}{\coth(1)[\frac{\cosh^2(1)}{8\phi_{Pt-NW}} + \frac{q}{kT} - G_R]} \tag{19}$$

Consequently, from Eqs. (19) and (4), the donor concentration of a single ZnO NW is given by

$$N_d = \frac{16\pi^2 m_e^* \varepsilon_r \varepsilon_o}{h^2 \coth^2(1)[\frac{\cosh^2(1)}{8\phi_{Pt-NW}} + \frac{q}{kT} - G_R]^2} \tag{20}$$

8. Some further discussion about the source of n-type conductivity in the ZnO NWs

Hydrogen impurities, V_o, Zn_i and their complexes have often been cited as the defects responsible for the source of n-type conductivity in the ZnO NWs.[33] However, the predominate source of donors in ZnO is still an open and unresolved question. Although the

increase of the PL intensity [in Fig. 6(b)] is correlated with the increase of the oxygen vacancies concentration, theoretical studies have indicated that V_o is a deep donor[34] and hence it is unlikely to be a source for the intrinsic n-type donors in ZnO. On the other hand, Zn_i has been revealed by first principle calculations to be a shallow donor.[34] However the theoretical models have also shown that Zn_i possess high formation energy and are unstable as they are fast diffusers and are mobile at room temperature.[35] Since our ZnO NWs were prepared by the CVD process at a high temperature of 950^{o}C without the use of any hydrogen gas and hydrogen easily migrates out of ZnO at high temperature,[36] it is also unlikely that hydrogen is the contributing factor to the n-type semiconducting conductivity of the ZnO NWs. The stoichiometric analysis of the ZnO NWs (in Section 3.2) implies an oxygen deficient state in the NWs where the concentration of the V_o and Zn_i defects is positively correlated with increase in the length and donor concentration of the synthesized NWs as calculated from the analytical model. Hence it is likely that the attractive interaction between V_o and Zn_i [36] lead to a stable defect pair at room temperature where the mobility of the Zn_i are greatly reduced in the crystal lattice.[34] In fact the V_o-Zn_i defect pair can be regarded as a Zn-antisite (Zn_o) defect and first principle investigations based on plane-wave pseudopotential method shows that under zinc rich conditions, the formation energy of Zn_o is comparable to V_o and it is a shallow defect.[37] Furthermore, the co-existence of the V_o and Zn_i defects in oxygen deficient ZnO could be a source of dominant donor with a resultant supply of high electron concentration.[36] Hence we believe that the V_o-Zn_i complex as defect pairs could lead to the incorporation of donor levels in the NWs and is the source of the n-type conductivity in the synthesized NWs.

References

1 L. J. Van der Pauw, *Philips Res. Rep.*, 1958, **13**, 1.
2 S.-H. Kim, S.-W. Jeong, D.-K. Hwang, S.-J. Park and T.-Y. Seong, *Electrochem. Solid St.*, 2005, **8**, G198.
3 W. L. Ong, C. Zhang and G. W. Ho, *Nanoscale*, 2011. (Advance article, DOI: 10.1039/c1nr10527b)
4 Y. He, J.-A. Wang, X.-B. Chen, W.-F. Zhang, X.-Y. Zeng and Q.-W. Gu, *J. Nanopart. Res.*, 2010, **12**, 169.
5 C.-L. Hsu, Y.-R. Lin, S.-J. Chang, T.-H. Lu, T.-S. Lin, S.-Y. Tsai and I.-C. Chen, *J. Electrochem. Soc.*, 2006, **153**, G333.
6 S.-P. Chang, C.-Y. Lu, S.-J. Chang, Y.-Z. Chiou, C.-L. Hsu, P.-Y. Su and T.-J. Hsueh, *Jpn. J. Appl. Phys.*, 2011, **50**, 01AJ05.
7 T.-J. Hsueh, C.-L. Hsu, S.-J. Chang, P.-W. Guo, J.-H. Hsieh and I.-C. Chen, *Scripta Mater.*, 2007, **57**, 53.
8 E. M. Likovich, K. J. Russell, E. W. Petersen and V. Narayanamurti, *Phys. Rev. B*, 2009, **80**, 245318.
9 X. H. Li, A. P. Huang, M. K. Zhu, Sh. L. Xu, J. Chen, H. Wang, B. Wang and H. Yan, *Mater. Lett.*, 2003, **57**, 4655.
10 H.-J. Jin, S.-H. Oh and C.-B. Park, *Appl. Surf. Sci.*, 2008, **254**, 2207.
11 J. Jie, A. Morita and H. Shirai, *J. Appl. Phys.*, 2010, **108**, 033521.
12 W. Water and S.-Y. Chu, *Mater. Lett.*, 2002, **55**, 67.
13 L. Wang, Y. Pu, Y. F. Chen, C. L. Mo, W. Q. Fang, C. B. Xiong, J. N. Dai and F. Y. Jiang, *J. Cryst. Growth*, 2005 **284**, 459.
14 A. L. Patterson, *Phys. Rev.*, 1939, **56**, 978.
15 K.-K. Kim, J.-H. Song, H.-J. Jung, W.-K. Choi, S.-J. Park and J.-H. Song, *J. Appl. Phys.*, 2000, **87**, 3573.
16 K. Vanheusden, W. L. Warren, C. H. Seager, D. R. Tallant, J. A. Voigt and B. E. Gnade, *J. Appl. Phys.*, 1996, **79**, 7983.
17 A. van Dijken, E. A. Meulenkamp, D. Vanmaekelbergh and A. Meijerink, *J. Phys. Chem. B*, 2000, **104**, 1715.
18 M. Ghosh and A. K. Raychaudhuri, *Nanotechnology*, 2008, **19**, 445704.
19 G. S. Huang, X. L. Wu, L. W. Yang, X. F. Shao, G. G. Siu and P. K. Chu, *Appl. Phys. A*, 2005, **81**, 1345.
20 J. K. Vassiliou, V. Mehrotra, M. W. Russell, E. P. Giannelis, R. D. McMichael, R. D. Shull and R. F. Ziolo, *J. Appl. Phys.*, 1993, **73**, 5109.
21 *Mechanics of Materials Volume 1 : An Introduction to the Mechanics of Elastic and Plastic Deformation of Solids and Structural Materials*, E. J. Hearn, Butterworth-Heinemann, Oxford, 3rd edn, 1997.
22 S. Hong, T. Joo, W. II. Park, Y. H. Jun and G.-C. Yi, *Appl. Phys. Lett.*, 2003, **83**, 4157.
23 A. N. Georgobiani and A. N. Gruzintsev, *Inorg. Mater.*, 2011, **47**, 107.
24 S.-K. Lee, S. L. Chen, D. Hongxing, L. Sun, Z. Chen, W. M. Chen and I. A. Buyanova, *Appl. Phys. Lett.*, 2010, **96**, 083104.
25 J. S. Reparaz, F. Gűell, M. R. Wagner, A. Hoffmann, A. Cornet and J. R. Morante, *Appl. Phys. Lett.*, 2010, **96**, 053105.
26 G. Pozina, L. L. Yang, Q. X. Zhao, L. Hultman and P. G. Lagoudakis, *Appl. Phys. Lett.*, 2010, **97**, 131909.
27 C. H. Chia, Y. J. Lai, T. C. Han, J. W. Chiou, Y. M. Hu and W. C. Chou, *Appl. Phys. Lett.*, 2010, **96**, 081903.
28 L. C. Lenchyshyn, M. L. W. Thewalt, D. C. Houghton, J.-P. Noël, N. L. Rowell, J. C. Sturm and X. Xiao, *Phys. Rev. B*, 1993, **47**, 16655.
29 *Physics of Semiconductor Devices*, S. M. Sze and K. K. Ng, Wiley, New York, 3rd edn, 2007.
30 N. Ashkenov, B. N. Mbenkum, C. Bundesmann, V. Riede, M. Lorenz, D. Spemann, E. M. Kaidashev, A. Kasic, M. Schubert, M. Grundmann, G. Wagner, H. Neumann, V. Darakchieva, H. Arwin and B. Monemar, *J. Appl. Phys.*, 2003, **93**, 126.
31 *History of Continued Fractions and Padé Approximants*, C. Brezinski, Springer, Berlin Heidelberg, 1991.
32 Ü. Özgür, Ya. I. Alivov, C. Liu, A. Teke, M. A. Reshchikov, S. Doğan, V. Avrutin, S.-J. Cho and H. Morkoc, *J. Appl. Phys.*, 2005, **98**, 041301.
33 F. Sun, C. X. Shan, S. P. Wang, B. H. Li, J. Y. Zhang, Z. Z. Zhang, D. X. Zhao, B. Yao, D. Z. Shen and X. W. Fan, *Appl. Surf. Sci.*, 2010, **256**, 3390.
34 R. Vidya, P. Ravindran, H. Fjellvåg, B. G. Svensson, E. Monakhov, M. Ganchenkova and R. M. Nieminen, *Phys. Rev. B*, 2011, **83**, 045206.
35 P. Erhart and K. Albe, *Appl. Phys. Lett.*, 2006, **88**, 201918.
36 Y.-S. Kim and C. H. Park, *Phys. Rev. Lett.*, 2009, **102**, 086403.
37 F. Oba, S. R. Nishitani, S. Isotani, H. Adachi and I. Tanaka, *J. Appl. Phys.*, 2001, **90**, 824.